Acta Materialia 297 (2025) 121373

Contents lists available at ScienceDirect

Acta Materialia

journal homepage: www.elsevier.com/locate/actamat

Enabling circularity of copper through nanoscale impurity control

Raymond Kwesi Nutor [a,*], Martina Ruffino [a], Adam Cohen Miles [a], Yug Joshi [a], Eric V. Woods [a], Mohammed Kamran Bhat [a], Syeda Ramin Jannat [b], Ubaid Manzoor [a], Isnaldi R. Souza Filho [a,c], Dierk Raabe [a,*], Baptiste Gault [a,b,*]

[a] Max-Planck-Institute for Sustainable Materials, Düsseldorf 40237, Germany
[b] Department of Materials, Imperial College London, London SW7 2AZ, UK
[c] Institut Jean Lamour, CNRS (UMR 7198), Université de Lorraine, Nancy F-54000, France

ARTICLE INFO

Keywords:
Copper
Lithium ion batteries
Atom probe tomography
Sustainability
Recycling

ABSTRACT

Copper (Cu) is essential to the electrification of society, yet primary Cu ores contain less than 1% metal, making mining insufficient to meet the demands of the clean energy transition. Recycling offers a viable alternative, reducing CO_2 emissions by up to 65%, but conductivity losses due to scrap-related impurities hinder its application in high-performance systems. In this work, we introduce a recycling strategy for Cu recovered from electric vehicle (EV) batteries, enabling direct and circular reuse. Through nanoscale analysis, we show that by gettering impurities into nanoparticles spaced approximately 40 nm apart, they become effectively "invisible" to conduction electrons. This self-cleaning mechanism maintains both electrical conductivity and mechanical integrity, turning detrimental impurities into functional alloying elements and facilitating the sustainable reuse of Cu.

1. Introduction

The discovery of copper (Cu) alloys marked a significant milestone in human history, ushering mankind out of the Stone Age into the Bronze Age and leading to applications ranging from plumbing to coinage throughout the ages. Today, Cu is essential for sustainable energy production and transmission due to its excellent electrical conductivity coupled with strength and formability [1,2]. The global Cu demand is expected to reach 53 million metric tons by 2050 (Fig. 1a) due to the push for decarbonization and digital innovation [2–5]. Yet, stringent environmental constraints and economic growth must be reconciled in that context [4]. This raises concerns about the criticality of Cu given its geochemical scarcity [1,2,6]. Therefore, additional Cu must enter the supply chain from secondary resources (i.e., scrap recycling) to enable the low-carbon energy transition [7,8]. Recycling Cu requires only about 10–15% of the energy needed for primary Cu production from ores [9] while avoiding environmental challenges such as water scarcity [10] and arsenic contamination [11] associated with mining Cu-containing ores. Given that the current end-of-life (EOL) Cu recycling rate is about 45%, a circular Cu economy is still far away [12,13]. While Cu used for cabling homes and industry is long-lived, Cu in the upcoming waves of short- and medium-lived consumer electronics, computers, and electrification products should also be targeted to establish circularity [9].

Electrifying the transportation sector through the adoption of electric vehicles (EVs) (Fig. 1b) offers an effective strategy to reduce greenhouse gas (GHG) emissions from mobility and to decrease air and noise pollution associated with internal combustion engine vehicles [14,15]. In lithium-ion batteries (LIBs), Cu is used as a current collector (CC) on the anode (usually graphite), maintaining electrical contact by transporting electrons generated at electrodes to external circuits, including the electric motor [16]. E-buses or E-trucks contain nearly 400 kg of Cu for electrical connections and 15–40 kg of Cu in the batteries (depending on battery chemistry) [16,17]. Since sulfide- and oxide-based Cu ores contain 0.1–2% Cu, only 1–20 kg of pure Cu can be extracted for every ton of ore mined [3]. Therefore, recycling Cu from the automotive sector presents an opportunity to boost Cu's sustainability, especially since global projections suggest that ~1.1 million batteries will reach EOL by 2030 (LIBs have a lifetime of around 10–15 years) [18,19]. Additionally, recycling EV battery scrap can prevent environmental problems such as soil pollution and fire hazards associated with improper battery disposal [20–22].

Recycling Cu involves specific metallurgical challenges compared to primary production, mainly arising from the heterogeneous chemical

* Corresponding authors at: Max-Planck-Institute for Sustainable Materials, Düsseldorf 40237, Germany.
E-mail addresses: r.nutor@mpie.de (R.K. Nutor), d.raabe@mpie.de (D. Raabe), b.gault@mpie.de (B. Gault).

https://doi.org/10.1016/j.actamat.2025.121373
Received 14 April 2025; Received in revised form 30 June 2025; Accepted 23 July 2025
Available online 25 July 2025

compositions of scrap Cu, the presence of various alloying elements and contaminants, and the complex microstructural changes that occur during recycling [23]. These challenges are especially difficult to circumvent because preserving chemical purity is vital for high-conductivity applications. Mixed or lower-grade scrap often contains detrimental impurities such as iron (Fe), nickel (Ni), cobalt (Co), manganese (Mn), and chromium (Cr) [24]. These (anti-)ferromagnetic solutes in solid solution can markedly degrade the electrical performance of Cu [25]. Elements such as lead (Pb), bismuth (Bi), and antimony (Sb) are particularly harmful during processing because they can form low-melting eutectics, leading to hot shortness, embrittlement, and intergranular cracking [26]. Aluminum (Al), silicon (Si), and zinc (Zn) are also common in recycled Cu feedstocks, but can often be partially removed through oxidation or drossing techniques [24]. However,

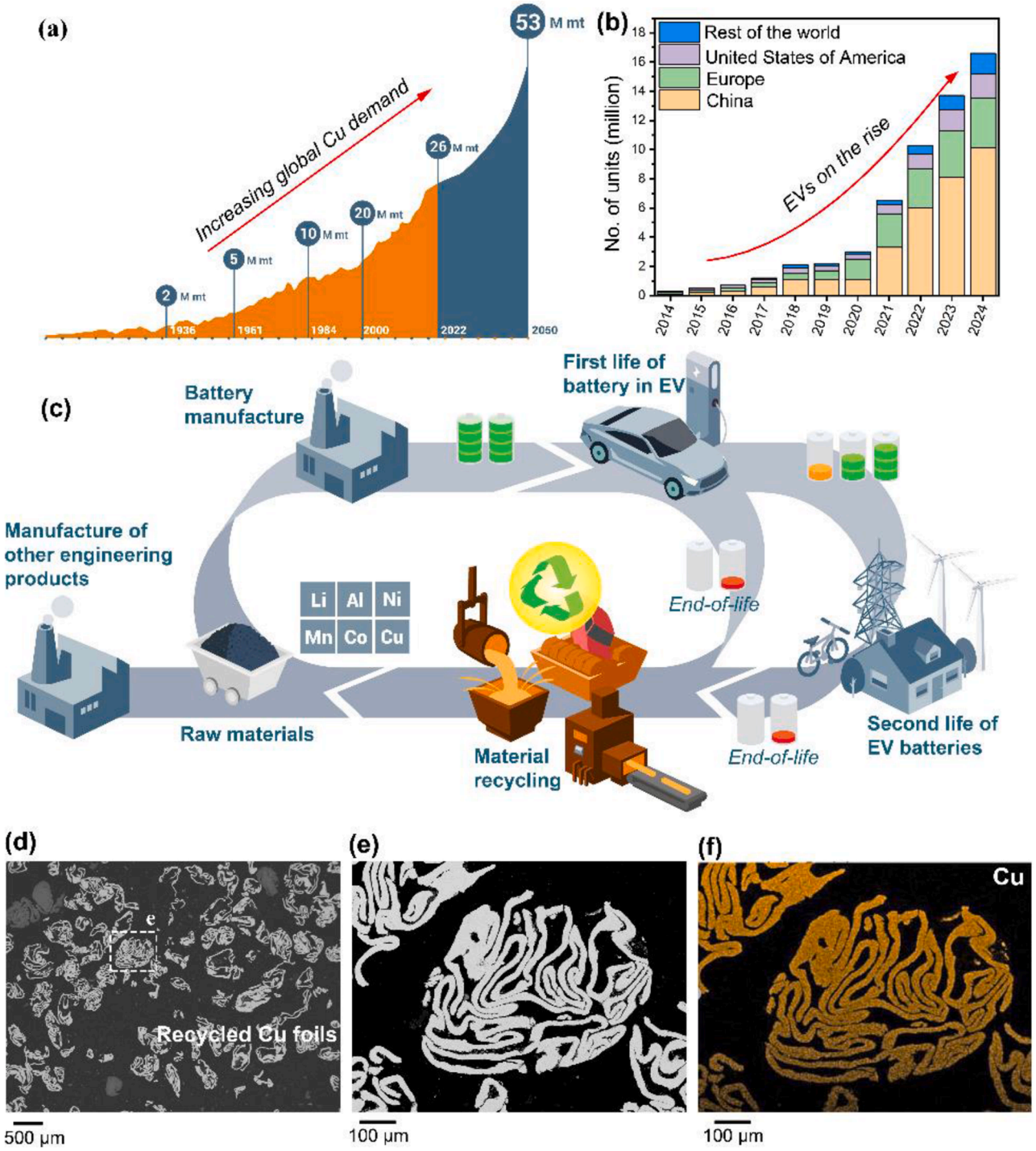

Fig. 1. The demand and recycling landscape for Cu from the EV sector. (a) Copper demand chart showing the annual Cu demand in 2050 to be greater than all Cu consumed from 1900 to 2022 (source: https://www.stocktitan.net/news/WTCRF/li3-lithium-announces-shareholder-approval-of-name-change-to-reflect-jj1sqve78mae.html). (b) Chart showing the rising EV sales in China, EU, USA, and the rest of the world (source: https://www.iea.org/data-and-statistics/charts/electric-car-sales-2012–2024). (c) Schematic representation of the circular economy of EV batteries, from material extraction to recycling practices (Adapted with permission from Refs. [34,35]). (d, e) Scanning electron microscope (SEM) micrograph of representative recycled Cu foils from EV batteries and corresponding (f) Energy dispersive X-ray spectroscopy (EDS) map of the foil showing the presence of Cu.

pyrometallurgical refining methods are inherently difficult to operate due to the imperative need for precise oxidation control during remelting [9]. Copper readily oxidizes to Cu_2O between 1065–1085°C, creating a low-melting eutectic capable of penetrating grain boundaries and becoming susceptible to hydrogen embrittlement via intergranular decohesion when hydrogen is present [27,28]. Thus, deoxidation with phosphorus (P) or lithium (Li) is essential for certain grades, such as Cu-HCP (high-conductivity phosphorus-deoxidized copper) [29]. During melting and solidification, copper typically develops columnar grains, attributed to its high thermal conductivity and low nucleation rate [30]. Impurities such as tin (Sn), Zn, and Ni tend to promote a transition from columnar to dendritic or cellular grain growth by altering the liquidus-solidus interval and increasing constitutional supercooling during recycling [24,30]. Moreover, these impurities can form second-phase particles (e.g., Cu_6Sn_5, Cu_3Sb, Ni_3Sn) that promote recrystallization by serving as nucleation sites, but can also act as stress concentrators, leading to cracks under cyclic thermal or mechanical stress [31,32].

Battery recycling for material reclamation faces several challenges. First, the diversity in LIB chemistry and structural designs complicates the recycling process as contamination from the other battery components is inevitable, resulting in complex mixed scrap streams [14]. Such contamination is typically undesirable for applications because it degrades the functional properties of the reclaimed material. This, therefore, calls for additional refining steps or metal dilution, which are expensive and defeat the purpose of sustainable recycling. In the case of Cu, important properties to be maintained for electrical transmission are high strength and conductivity. However, recycled Cu often contains impurity solutes, crystalline defects such as dislocations and vacancies, as well as microstructural interfaces, including twins, stacking faults, and grain or phase boundaries. While these features can enhance mechanical properties, such as strength and ductility through defect-mediated strengthening mechanisms, they also serve as potent sources of inelastic electron scattering, thereby significantly reducing electrical conductivity [33]. Achieving an optimal balance between mechanical and functional properties necessitates a comprehensive investigation of the recycled Cu's microstructure, chemistry, and performance across multiple length scales.

Fig. 1c shows a model of the sustainable circular economy of LIBs from raw material extraction to EOL [34,35]. The current LIB recycling industry prefers to handle production scraps as the chemistries are known and with no contamination from usage. Depending on their state of health, EV batteries can be repurposed for second-life use as stationary energy storage for grid balancing and powering light transport devices like scooters and e-bikes. Once the batteries (from first and second life) reach their EOL, battery cells must be discharged and disassembled for material separation [14]. Recycling aims to reclaim some critical materials, some of which are used as secondary raw materials for battery production (i.e., direct recycling) or to manufacture other engineering products, often with downcycled material grades. The current battery recycling practice uses, in part, mechanical, pyrometallurgical, or hydrometallurgical processes for material recovery, but more efficient and sustainable technologies need to be developed in this sector [34,36–38].

Here, we demonstrate the recycling of Cu material from EOL batteries with lithium-nickel-manganese-cobalt-oxide (NMC811) cathode, following physical separation (viz., shredding and density-based sorting). Fig. 1d, e show the scanning electron microscope (SEM) images of the recycled Cu foils with the corresponding energy-dispersive X-ray spectroscopy (EDS) map (Fig. 1f), revealing the uniform distribution of Cu at the microscale. The Cu foils were compacted into pellets before being cast and then subjected to homogenization, hot-rolling, cold-rolling, and annealing. To elucidate the influence of impurities on the mechanical and functional properties of recycled Cu, advanced characterization techniques – including electron backscatter diffraction (EBSD), transmission electron microscopy (TEM), and atom probe tomography (APT) – were employed to probe the microstructure down to the near-atomic scale.

2. Methods

2.1. Materials preparation

First, pellets were produced from scrap Cu foils obtained from an industrial partner. The chemical composition (wt.%) of the scrap Cu foil according to Inductively Coupled Plasma (ICP) wet chemical analysis is shown in Table 1. The pellets were melted in a vacuum induction furnace under a high-purity argon (Ar) atmosphere. The ingots were remelted five times to ensure chemical homogeneity. The melted ingots were cast into a mold measuring 100 mm × 20 mm × 20 mm (length × width × thickness). The cast slab was then homogenized at 1000°C for 6 h and water quenched. The homogenized sample was hot-rolled at 1000°C to achieve a 50% reduction in thickness. After hot rolling, the Cu sheet was cold-rolled to an 80% thickness reduction, resulting in a final thickness of 2 mm. Two annealing protocols were used to produce different grain sizes after cold rolling. The cold-rolled sheets were annealed at either 450°C or 550°C for 1 h, followed by water quenching. For simplicity, the final states of the samples were labeled as "Cu450" and "Cu550".

2.2. Microstructure characterization

The microstructures of the investigated samples were characterized by backscattered electron (BSE) imaging using a Zeiss-Merlin scanning electron microscopy (SEM). Electron backscattered diffraction (EBSD) and energy dispersive spectroscopy (EDS) analyses were conducted in the same SEM equipped with the EDAX software. EBSD data was analyzed using the OIM software (Version 9). Transmission electron microscopy (TEM) analysis was carried out in an aberration-corrected FEI Titan Themis 60–300 operated at 300 kV. Atom probe tomography (APT) specimens were prepared from the bulk samples in a FEI Helios Dual Beam Xe-Plasma focused ion beam (FIB). A local electron atom probe (LEAP 5000XR, Cameca) was used in the laser-pulsed mode for the APT experiments. All APT experiments were performed at 60 K, 125 kHz pulse rate, and 40 pJ pulse energy. APT data was analyzed using the APsuite software (version 6).

2.2.1. Estimation of precipitate volume fraction

The distinct differences in matrix and precipitate compositions allow for the estimation of the volume fractions of the precipitates from the APT datasets using the Lever rule expressed as:

$$C_n = V_p C_p + (1 - V_p) C_m$$

Where C_n is the overall composition of the APT tip, C_p is the composition of the precipitates, C_m is the composition of the matrix and V_p is the volume fraction of the precipitates. A plot of $(C_n - C_m)$ against $(C_p - C_m)$ yields a straight line with the slope as V_p, similar to the equation of a straight line.

2.2.2. Estimation of particle size

The Nearest Neighbor Distribution protocol in the APsuite software (version 6) is first used to determine the maximum fixed distance (d_{max}) between the clusters. A fifth-order nearest-neighbor distribution is then used to define the large clusters which are the precipitates. Other atoms within some distance L greater than d are assumed as members of the cluster while taking clusters above a certain minimum number of solute atoms (N_{min}). The average volume of the clusters (V_{extent}) is then estimated by using the cluster-finding protocol in the APsuite software (version 6). Since the precipitates are spherical, the average particle size is then estimated using the equation for the volume of a sphere.

Table 1
Composition of as-received Cu scrap by wet chemical analysis.

Elements	Al	C	Co	Fe	Li	Mn	Ni	P	Si	Zn	Cu
Scrap Cu	0.19	0.53	0.13	0.17	0.11	0.18	0.26	0.068	<0.02	0.11	Bal.

2.2.3. Estimation of interparticle spacing

The interparticle spacing between the precipitates is also estimated using the cluster-finding protocols in the APsuite software (version 6) described above. The parameters are all set by following the procedure described above and elsewhere [39]. The positions of the particles obtained in 3D are then used to estimate the 2D first nearest neighbor distance between the particles. However, we note this nearest neighbor distance is taken from the center of the particles and must be converted to the distance between the spheres. This is simply done by using the expression ($d_{IP} = d_{center} - 2R$), where d_{IP} is the average interparticle spacing, d_{center} is the average interparticle spacing between the centers of two spherical particles and R is the average radius of the precipitates.

2.3. Mechanical property measurements

Flat-dog bone specimens of 20 mm total length (gauge length = 12 mm, gauge width = 2 mm, and thickness of 2 mm) were used for room temperature uniaxial tensile tests at a constant strain rate of 1×10^{-3} s^{-1}. A digital image correlation (DIC) method (Aramis system) was used to evaluate the local strain evolution during tensile testing. The tensile specimens were ground and polished to a mirror finish before the tensile tests. The tensile tests were repeated three times for each annealing condition to ensure reproducibility.

Nanoindentation tests were conducted using a diamond Berkovich tip (Synton-MDP AG, Switzerland) attached to a KLA G200 Nanoindenter XP head. Before testing, the tip area function was calibrated using fused silica. Room temperature measurements were performed using the continuous stiffness measurement (CSM) method, yield hardness (H), and elastic modulus (E) values as a function of increasing penetration depth. The maximum allowable drift rate was set to 0.05 nm s^{-1} and the load rate was fixed at 0.05 s^{-1}. Hardness (H) and elastic modulus (E) values were extracted using the Oliver and Pharr method, with the maximum indentation depth set to 1000 nm.

2.4. Electrical resistivity measurements

The electrical resistivities of the samples were probed in a LINKAM-HFS600 system with four tungsten probes. Before testing, all samples were ground and polished to a mirror finish without noticeable scratches. The resistivity was determined following the standard Van der Pauw method [40]. Sample shape or probe positioning asymmetries were corrected as outlined by Bishara *et al.* [41]. At least three specimens were tested for each condition.

2.4.1. Estimation of electrical resistivity

The underlying theories and equations used to model the resistivity in the modified code are based on fundamental principles of solid-state physics and materials science. This considers the different microstructural and atomic contributions to the electrical resistivity. Here, a model composition $CuFe_{0.11}Ni_{0.27}Co_{0.05}Mn_{0.11}$ (at.%) based on the chemical information from the APT analysis is used to estimate the electrical resistivity at fixed grain sizes, while varying (a) the amount of the main impurity element (Fe) and (b) the volume fraction of the nanoparticles. The total resistivity (ρ_{total}) of the copper alloy is the sum of the intrinsic resistivity of pure copper, the resistivity contributions from impurities, nanoparticles, and grain boundaries.

Intrinsic resistivity of pure Cu: $\rho_{Cu}(T) = \rho_0(1+\alpha(T\text{-}T_0))$, where ρ_0 is the intrinsic resistivity of pure Cu, α is the temperature coefficient of resistivity and T_0 is the reference temperature (often taken as room temperature, 293.15 K).

Resistivity contribution from impurities (solid solution): $\rho_{solute} = \sum i(A_i \cdot c_i)$, where A_i is the empirical constant specific to each impurity element i (represents the resistivity increase per atomic percentage of the impurity) and c_i is the atomic percentage concentration of impurity i.

Resistivity contribution from nanoparticles: $\rho_{np} = B \times (f_{np}/d_{np})$, where B is the empirical constant representing the strength of the scattering due to nanoparticles, f_{np} is the volume fraction of nanoparticles and d_{np} is the diameter of nanoparticles.

Resistivity contribution from grain boundaries: $\rho_{GB} = C_{grain}/d_{grain}$, where C_{grain} is the empirical constant representing the impact of grain boundaries on resistivity and d_{grain} is the average grain size of the Cu matrix.

2.5. Electrochemical measurements

The Cu450 and Cu550 current collectors (CCs) were first cut to a disc geometry (150 μm thick, ϕ = 10 mm) [42]. To prepare the graphite electrode, a conventional 90:2:8 mass ratio of 5-μm graphite powder (Graphene Supermarket, 99%), Super P carbon black (Imerys, >99%) and polyvinylidene fluoride (PVDF, Merck) was used. The slurry was prepared inside a fume hood, using N-methyl-2-pyrrolidone (NMP, Merck, anhydrous 99.5%) as the solvent and mixed with a Thinky mixer (ARM-310, Intertronics) to achieve a homogeneous slurry. The slurry was then cast to 100 μm using a pipette and an adjustable wet film applicator. Each 150 μm-thick (Cu450 and Cu550) CC was placed between two glass plates of the same thickness to achieve a uniform cast. The electrodes were dried under a fume hood at 80°C overnight and subsequently under a vacuum at 80°C, before being transferred into an Ar glovebox.

A symmetrical configuration was used for the electrochemical impedance spectroscopy. Two similarly prepared synthesized graphite electrodes were used in a Swagelok cell (Cambridge Energy Solutions). The cell was prepared in a glovebox with 1 mm steel spacers and was filled with 1 M LiPF6 in EC:DMC (v/v, Mersk) electrolyte.

The galvanostatic dis-/charging was done in a CR2032 half cell. The cells were prepared inside an Ar glovebox using the synthesized graphite (ϕ = 10 mm) as the cathode and Lithium foil as the anode. Along with these components, a cell guard PP separator, one stainless steel spring (MTI), and two spacers (1 mm total thickness, MTI) were used, complete with 100 μL of 1 M $LiPF_6$ in EC:EMC (50:50 v/v, Merck) electrolyte. Following assembly, the coin cells were left overnight before electrochemical testing was carried out under ambient conditions.

Galvanostatic cycling and electrochemical impedance spectroscopy (EIS) tests were performed using a Biologic VSP-300 potentiostat. EIS was carried out in the range of 7 MHz – 1 Hz frequency range at 10 mV sinus amplitude at OCV (~2 V vs Li/Li^+). Charging and discharging were performed in the voltage range of 1.5 V – 0.05 V. One slow formation cycle at C/20 was initially carried out to establish a stable solid-electrolyte interphase (SEI), followed by 2 cycles at C/7 and 3 cycles at C/3.

3. Results

3.1. Starting microstructure

Differential scanning calorimetry (DSC) analysis (Fig. 2a) of the cast sample shows a single exothermic event related to melting, with no discernible solid-solid phase transitions. The melting point is estimated to be 1074 ± 2.2°C, which is about 10°C lower than that of pure Cu

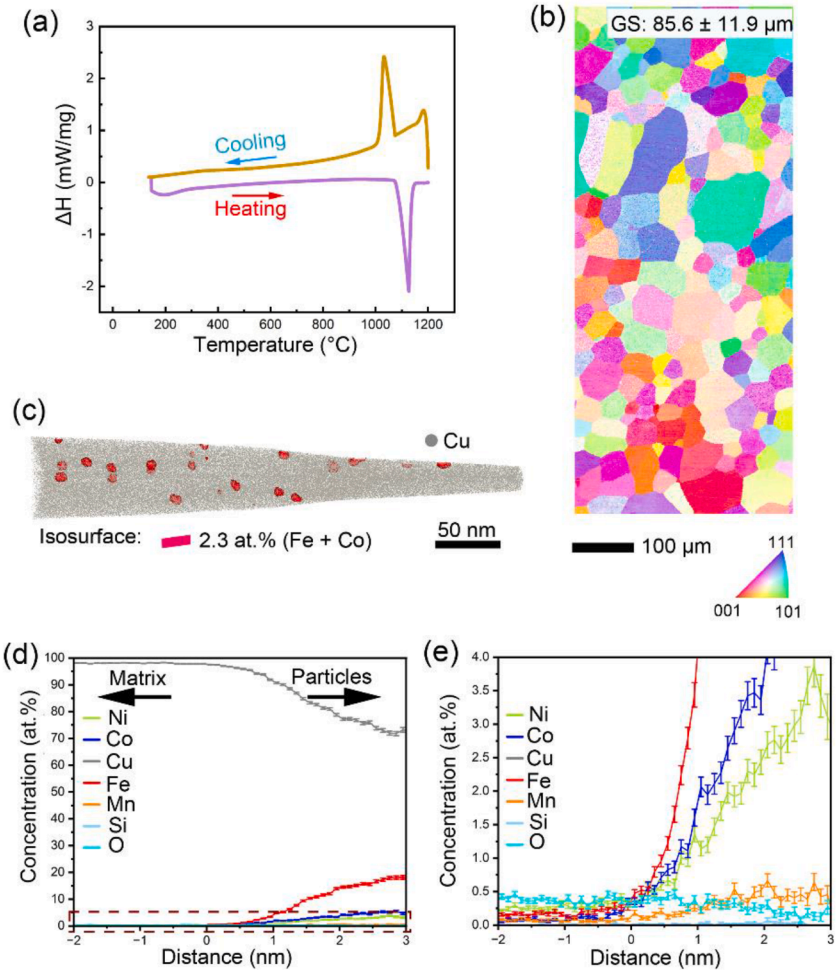

Fig. 2. (a) DSC heating/cooling curves of the as-cast sample showing the melting and solidification processes. (b) EBSD inverse pole figure (IPF) map of the as-cast sample. (c) 3D reconstruction map revealing the nanoscale elemental distribution in the as-cast recycled Cu. (d) Proximity histogram showing the compositional difference between the matrix and nanoparticles. (e) Corresponding zoomed-in image of the selected region in (d).

(1085°C), indicating impurity-induced melting point depression. Electron backscatter diffraction (EBSD) analysis (Fig. 2b) indicates a single-phase face-centered cubic (FCC) structure of the cast sample with an average grain size of 85.6 ± 11.9 μm. To map the distribution of impurities within the raw material arising from contamination during battery recycling, we used atom probe tomography (APT), with its high chemical sensitivity and nanoscale spatial resolution [43]. The elemental distribution in the as-cast sample already shows near-spherical particles within the Cu matrix, revealed by the 2.3 at.% (Fe + Co) isoconcentration surface (Fig. 2c). The mass spectra (Fig. S1) identified Fe, Mn, Si, O, Ni, Co, and Si as the main impurities introduced during recycling. These impurities are also present in the annealed samples, which will be discussed later. Composition profiles calculated as a function of distance to the isosurface [44] in Fig. 2c (i.e., proximity histograms) are shown in Fig. 2d, e . Trace amounts of the impurities (<0.3 at.%) in the Cu matrix are seen, while the particles show significant enrichment in Fe (18.08 at.%), Co (5.15 at.%), and Ni (3.38 at.%). The chemical compositions of the matrix and particles of the as-cast sample are summarized in Supplementary Table 1.

3.2. Mechanical and electrical properties

CCs are exposed to compressive and tensile forces in operation, where mechanical loads (vibrations and shocks) are exerted externally on the batteries (such as in electric vehicles). Moreover, the electrode materials expand and contract during charge and discharge cycles, generating mechanical stresses that could cause delamination of active materials from the collector, bending, or cracking of the thin metal foils used in CCs, resulting in short circuits or structural failure [45–47]. Thus, understanding and managing mechanical stress in batteries is crucial for improving performance, durability, and safety. Fig. 3a plots the engineering stress-strain curves for the Cu450 and Cu550 samples. The Cu450 sample has a yield strength (σ_y) of 138 ± 4.6 MPa, an ultimate tensile strength (σ_u) of 233 ± 3.2 MPa, whereas the Cu550 sample exhibits σ_y = 109 ± 5.8 MPa and σ_u = 215 ± 2.8 MPa. Both samples undergo a prolonged strain hardening, resulting in high elongations to fracture of 84.7 ± 1.2% and 87.1 ± 0.9% for the Cu450 and Cu550 samples, respectively. The yield strength of the commercial (18 μm thick) Cu CC foil, serving as reference material in this study is 79 MPa [48]. Furthermore, nanoindentation measurements (Fig. S2) show that both Cu450 and Cu550 materials exhibit good resistance to localized plastic deformation, an approximate qualitative metric for formability.

We measured the electrical resistivities of the samples and compared them to those of commercial CCs (Fig. 3b) [47]. The resistivity increases from 1.74 μΩ·cm for the commercial Cu CC to 2.68 μΩ·cm (Cu550) and 3.94 μΩ·cm (Cu450), respectively. Notably, the Cu550 sample exhibits a significantly lower electrical resistivity compared to commercial Al CCs, indicating the potential viability of recycled Cu as an alternative current collector material [47]. Furthermore, as Cu is the standard anode CC, the recycled Cu samples exhibit superior electrical conductivity – reflected in lower resistivity values – relative to other commonly considered negative CC materials such as Ti, Fe, and Ni [49].

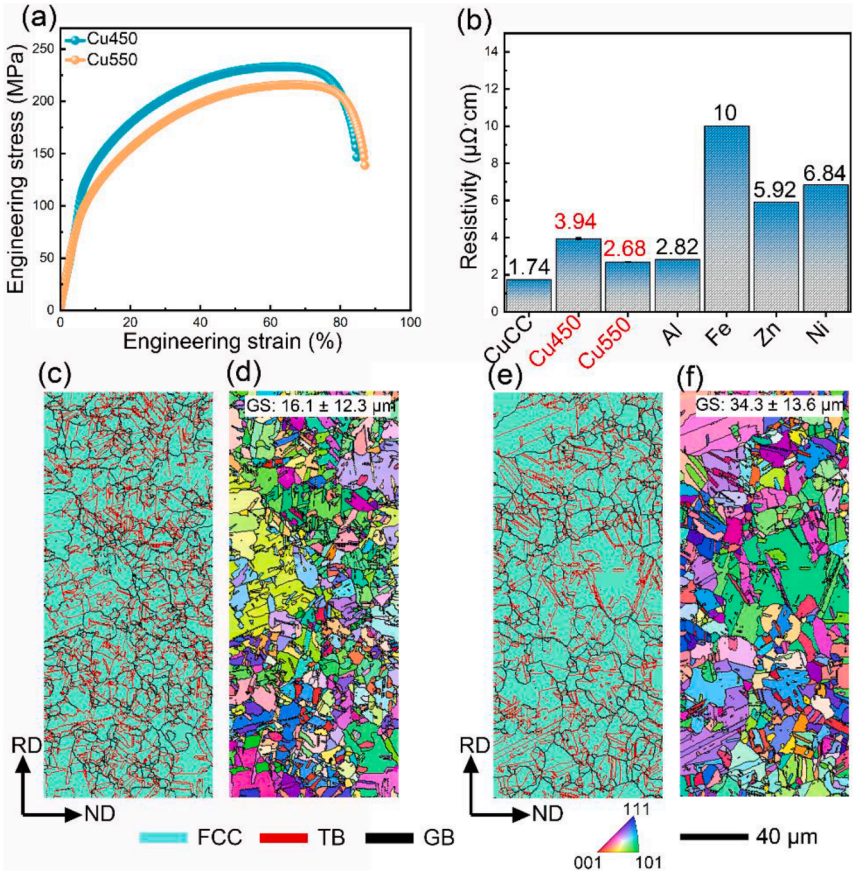

Fig. 3. Mechanical behavior and mesoscale microstructure of the Cu450 and Cu550 samples. (a) Tensile stress-strain curves and (b) Electrical resistivity of the recycled Cu CCs compared to other commercial CCs [47]. (c–f) EBSD phase and inverse pole figure (IPF) maps showing the recrystallized grains of the Cu450 and Cu550 samples with respect to the normal direction. The phase maps reveal a single-phase FCC structure. Black lines refer to the grain boundaries (GBs), and red lines refer to "TB" which denotes twin boundaries. (ND = normal direction; RD = rolling direction).

Fig. 3c–f show the mesoscale microstructure of the Cu samples as determined by EBSD analysis. EBSD phase maps (Fig. 3c and 3e) confirm the FCC structure of the Cu450 and Cu550 samples. The average grain sizes (excluding annealing twin boundaries) of the Cu450 and Cu550 samples are 16.1 ± 12.3 μm and 34.3 ± 13.6 μm, respectively. For comparison, the average grain size of a high-purity (99.99%) commercial Cu CC with 18 μm thickness is estimated as 830 ± 37.4 nm (Fig. S3a). Grain refinement typically increases strength by introducing a higher density of grain boundaries acting as effective barriers against dislocation motion (i.e., Hall-Petch effect) [50]. However, in the case of the 18-μm-thick commercial Cu CC with ultrafine grain size, its low yield strength (79 MPa) [48] relative to recycled Cu is attributed to the low dimensionality of the sample (thin foil).

3.3. Nano-structural and compositional analysis

Since grain boundaries (GBs) are prone to segregation by solutes [51], we first analyzed the GB elemental segregation in the Cu550 sample (Fig. 4a). The 1D compositional profile (Fig. 4b) along the GB shows substantial enrichment of O (up to 4.4 ± 0.96 at.%) at the GB (around 5 nm in the thickness direction). We then analyzed the elemental distribution by APT in the grain interior. Fig. 4c shows the 3D reconstruction of the elemental distribution in the Cu550 sample. Using isoconcentration surfaces delineating regions containing over 5 at.% Fe and 2 at.% Co, precipitates of near-spherical shape are revealed (Fig. 4d). The one-dimensional compositional profiles calculated as a function of the distance to these isosurfaces [44] (Fig. 4e) and its corresponding close-up analysis (Fig. 4f) show that these nanoprecipitates are enriched in Fe (30.32 at.%) and Co (8.01 at.%). Meanwhile, only trace amounts of Fe (0.08 at.%), Co (0.03 at.%), and Ni (0.27 at.%) are in the matrix.

The Cu450 sample contains similar spherical nanoprecipitates enriched in Fe (37.88 at.%) and Co (15.11 at.%) shown in Fig. S4. The amounts of Fe and Co in the matrix are 0.11 at.% and 0.04 at.%, respectively, which are slightly higher than those in the Cu550 sample. GB analysis also shows up to 4.7 ± 0.97 at.% of O at a GB of the Cu450 sample (Fig. S4). As a reference, the chemistry of the commercial Cu CC was also analyzed by APT (see Fig. S3). As anticipated, only trace amounts of Si and O are seen, with no precipitates present. We then analyzed the distribution of solute elements at a GB of the commercial Cu CC and observed no prominent O segregation at the GB relative to the grain interior (Fig. S3). The average chemical compositions of all the samples are provided in Supplementary Table 1. In the Cu450 sample, APT analysis reveals that the average particle size is 3.4 ± 0.6 nm, the average volume fraction of the precipitates is ~1.35%, and the interparticle spacing is about 9.2 nm. In the Cu550 sample, the precipitate volume fraction is ~0.15% with an average particle size of 5.4 ± 1.9 nm and an average interparticle spacing of ~40.8 nm. A summary of all relevant microstructural information is shown in Supplementary Table 2.

A transmission electron microscopy (TEM) image of a larger, near-spherical nanoprecipitate embedded in the FCC Cu matrix in Cu550 is displayed in Fig. 4g. At high resolution, multiple twinning interfaces are visible in the precipitate (Fig. 4h). The precipitate displays a 3R (i.e., three-layer stacking of close-packed planes with rhombohedral Bravais lattice) crystal structure according to the corresponding fast Fourier transform (FFT) image (Fig. 4i). Internal boundaries of the precipitate visible in the TEM images (Fig. 4g and 4h) are identified as twin

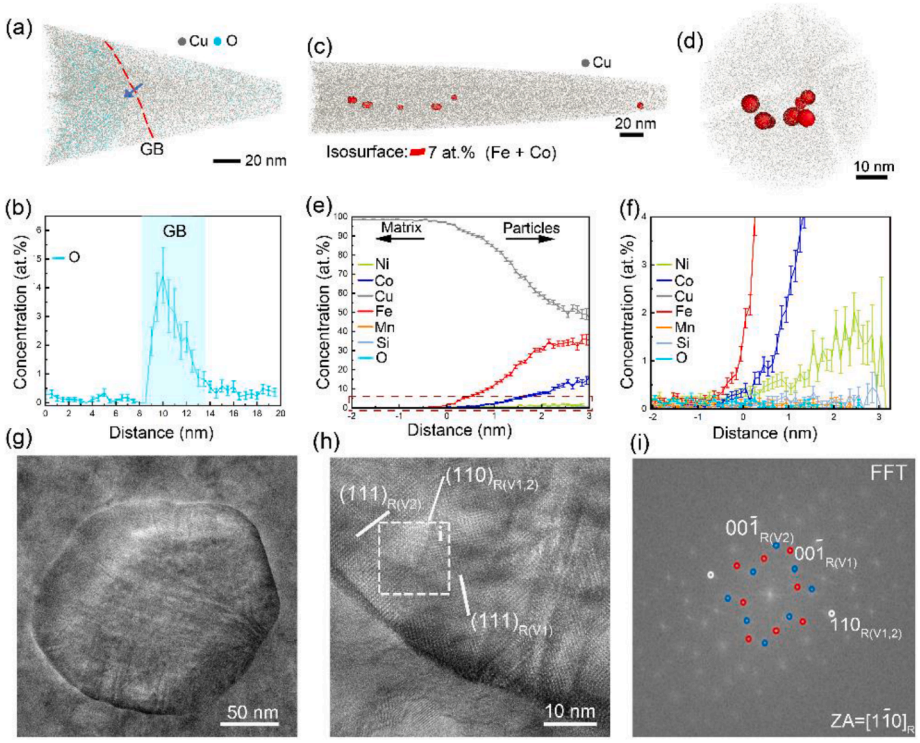

Fig. 4. APT analysis and nanoscale structural characterization of Cu550 sample. (a) 3D reconstruction map of APT tip with GB. (b) 1D compositional profile indicating oxygen segregation across the GB. (c) 3D reconstruction map revealing the elemental distribution of Cu with impurity atoms. (f) Reconstruction map from (C) in the z-view showing FeCo-rich nanoparticles in the FCC matrix. (e) 1D proximity profile displaying the compositional changes between the matrix and nanoparticles. (f) Corresponding zoomed-in image of the region in (E) indicated by the dashed rectangle. (g) BF-TEM image depicting nanoprecipitate embedded in FCC matrix. (h) High-resolution TEM image showing the matrix-nanoparticle interface and two twin variants in the nanoparticle. (i) Corresponding Fast Fourier Transform (FFT) pattern taken from the dashed region in (h) depicting the relationship between the twin variants.

interfaces through analysis of the corresponding FFT image of an area including two regions with common $[1\bar{1}0]_R$ zone axis (inset of Fig. 4h): overlapping 110_R spots for the two regions confirm that the interface plane is a mirror plane. The precipitate thus presents rhombohedral $\{110\}_R$ twins. In comparison, the nanoprecipitates observed in the Cu450 sample (Fig. S5) exhibit a characteristic 9R structure, defined by a nine-layer stacking sequence. This structure can be conceptualized as resulting from the periodic insertion of stacking faults every three hexagonal close-packed layers within a 3R framework, thereby producing the observed nine-layer periodicity. The presence of these stacking faults is corroborated by the faint streaks visible in the corresponding fast Fourier transform (FFT) image (inset of Fig. S5b). In contrast to the 3R precipitates, the 9R variants are free of twinning. It is noteworthy that the formation of both 3R and 9R precipitates has been widely associated with martensitic transformation pathways [52].

3.4. Integration into a battery cell

To assess the electrochemical performance of the recycled Cu, coin and symmetric cells were fabricated using Cu450 and Cu550 samples as current collectors, along with commercial graphite as the anode active material. Details of the cell preparation and experimental parameters are included in the Methods section. Fig. 5a shows the electrochemical impedance spectroscopy (EIS) of the symmetrical graphite anode using Cu450 and Cu550 as the current collectors. The bulk resistance/impedance from the electrodes is shown by the purple and green semicircles for Cu450 and Cu550, respectively. The Cu550 electrode has ca. 4.5 times higher conductivity. These electrodes were further tested in

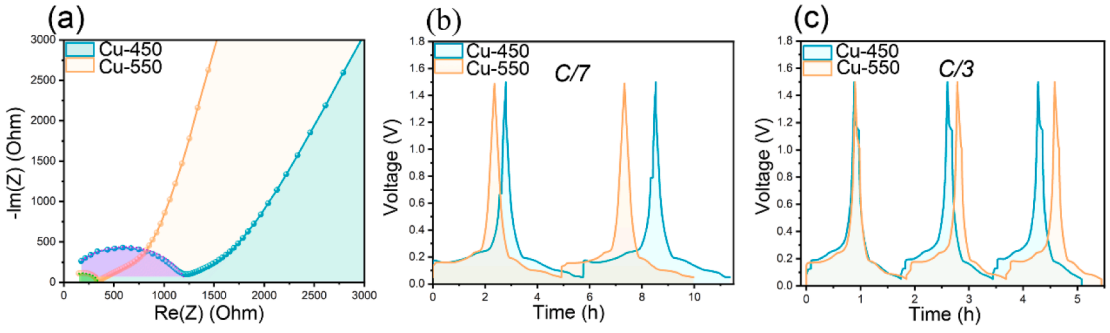

Fig. 5. Electrochemical impedance spectroscopy (EIS) and performance of the recycled Cu CC. (a) Electrochemical impedance spectroscopy (EIS) measurements comparing the impedance response for the Cu450 and Cu550, displaying distinct charge-transfer conductivity. The reduced charge transfer conductivity suggests enhanced ionic transfer from the electrolyte to the graphitic anode when Cu550 CC is used. (b-c) Galvanostatic charge-discharge profiles at different C-rates (C/7 and C/3) comparing the electrochemical rate performance between the samples Cu450 and Cu550.

a half-cell configuration at two different C-rates to test the performance of the battery produced using recycled copper as the current collector.

Fig. 5b and 5c present representative galvanostatic charge–discharge profiles of the graphite half-cells at current rates corresponding to C/7 and C/3, equivalent to complete charge and discharge durations of 7 h and 3 h, respectively. The electrochemical performance aligns with the EIS results: at lower charge rates, the Cu450 sample exhibits higher capacity, whereas at higher charge rates, the Cu550 sample outperforms Cu450. This response is likely attributed to the enhanced electrical conductivity of the Cu550 current collector, which facilitates improved charge transport under high-rate conditions.

4. Discussion

4.1. Microstructural influence on electrical resistivity

The fundamental challenge of Cu recycling from spent batteries lies in impurity incorporation from other cell components, which can significantly influence microstructural evolution and degrade electrical conductivity. Our analysis identifies Co, Ni, Mn, and Fe as the principal impurity elements present in the recycled Cu, consistent with their origin from NMC cathode or stainless steel casings [14]. While these impurities can enhance the mechanical strength of Cu through solid solution strengthening, they simultaneously act as effective inelastic electron-scattering centers. This effect arises from their strong (anti-) ferromagnetic spin coupling. Mn exhibits antiferromagnetic tendencies while Fe, Co, and Ni are ferromagnetic, leading to pronounced spin-disorder scattering and, consequently, a significant reduction in electrical conductivity [25]. The resistivity coefficients of the four main solute contaminants vary quite significantly in the literature within the following ranges [53,54]: 10.6–12.0 μΩ·cm per 1 at.% Fe; 2.9–3.4 μΩ·cm per 1 at.% Mn; 0.6–7.3 μΩ·cm per 1 at.% Co; and about 1.2 μΩ·cm per 1 at.% Ni, all of which apply to the solid solution matrix. From the theoretical point, the resistivity was calculated based on the composition of the APT-measured Cu matrix solid solution of the two samples. Fig. 6a illustrates the effect of Fe concentration on the electrical resistivity of a Cu solid solution. As the Fe amount increases from 0.1 at.% to 1 at.%, the resistivity increases rapidly from ~20 μΩ·cm to ~35 μΩ·cm, highlighting the strong scattering effect of Fe impurities in the Cu matrix. For perspective, pure copper, according to the International Annealed Copper Standard (IACS), exhibits 100% electrical conductivity – equivalent to 0.581 $S \cdot cm^{-1}$ or a resistivity of 1.72 μΩ·cm at room temperature. In comparison, the measured resistivity of the Cu550 sample is 2.68 μΩ·cm. This nearly six-fold increase can be largely attributed to impurity-driven electron scattering, where even a minor addition of 0.1 at.% Fe in the Cu matrix can elevate the resistivity considerably, given Fe's resistivity coefficient in Cu (~11.3 μΩ·cm). As a result, the electrical conductivity drops by approximately 40% relative to pure Cu, highlighting the pronounced sensitivity of Cu's electrical performance to dilute impurity concentrations.

Removing these impurities from the Cu solid solution phase and partitioning them into secondary-phase precipitates appears as the most promising strategy for thermodynamically "self-cleaning" the Cu matrix of recycled battery materials. The term self-cleaning is here used for two main reasons: First, the nanoparticles undergo spontaneous "self-assembly", i.e., thermal activation facilitates diffusion-driven nucleation and growth, processes that are thermally activated and energetically favored based on the system's phase equilibria. From APT analysis (Fig. 2c–e), we see that FeCo-rich nanoparticles are present even in the as-cast state, indicating inherently low solubility of these elements within the Cu matrix. Second, the thermodynamically driven partitioning of impurity solutes from the solid solution into discrete precipitates actively purifies the Cu matrix to improve its compositional integrity. In this context, scattering theory suggests that a spacing between precipitates larger than the electron mean free path determined by ambient temperature phonon scattering [55] should optimize conductivity. The mean free path of conduction electrons in Cu at room temperature due to inelastic phonon scattering is 40–50 nm under standard conditions [56]. Nanoprecipitates act as electron-scattering centers, with their contribution to electrical resistivity being inversely related to their size and directly proportional to their volume fraction [25,57].

According to the APT analysis, the average particle spacing between the nanoprecipitates is ~9.2 nm in the Cu450 sample and ~40.8 nm in the Cu550 sample. Given that the electron mean free path at room temperature exceeds the average interparticle spacing in the Cu450 sample (~9.2 nm) by approximately a factor of four, significant electron scattering at particle-matrix interfaces is expected. In contrast, the larger interparticle spacing in the Cu550 sample (~40.8 nm) closely matches the intrinsic electron mean free path in pure Cu limited by phonon scattering, suggesting minimal additional scattering from nanoprecipitates in this case [56]. The electron scattering is hence determined primarily by the matrix phonons in Cu550 as the "self-cleaned" matrix from which the contaminants escaped and partitioned into the nanoparticles appears as rather "pure Cu" to the electrons. This suggests that the contribution to the electron scattering at the matrix-particle interfaces becomes "unseen" to the conduction electrons. In other words, any particle spacing equal to or larger than the phonon-determined electron mean free path does not harm the material's electrical conductivity beyond the level set by phonon scattering. While the resistivity increases with the volume fraction of nanoprecipitates due to interface scattering,

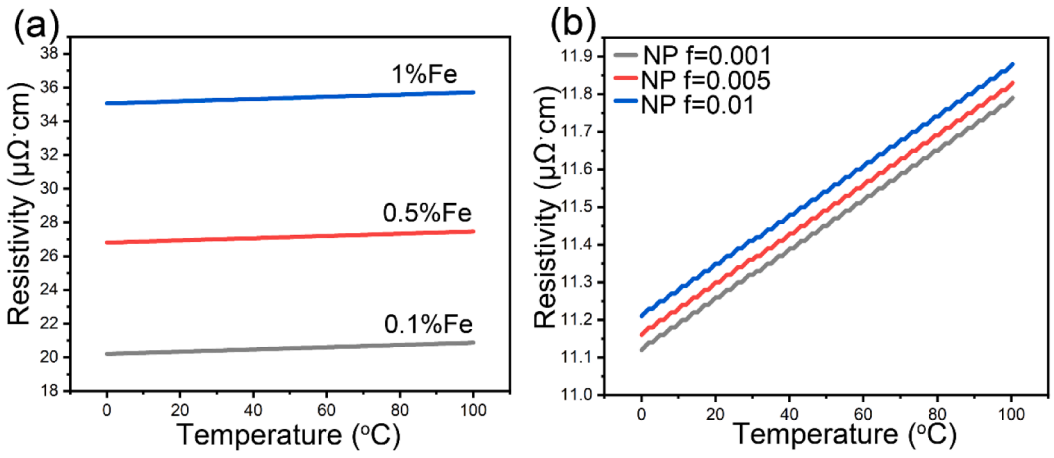

Fig. 6. Theoretical estimation of the resistivity. (a) Effect of Fe solute amount in the matrix on the bulk resistivity. (b) Influence of volume fraction of nanoprecipitates on bulk resistivity.

Fig. 6b indicates that this contribution is comparatively minor (i.e., a second-order effect). Apart from the matrix-precipitate interface being an electron-scattering site, lattice defects inside the precipitates can also cause inelastic electron scattering [31,58]. The 9R nanoprecipitates in the Cu450 sample contain stacking faults, while twins are present in the 3R nanoprecipitates of the Cu550 sample. Since the carrier scattering by twin interfaces is an order of magnitude lower than that of stacking faults, the resistivity of the 9R nanoparticles is higher than that of the 3R nanoparticles [59,60]. However, because of their low volume fractions, the nanoprecipitate effect on the electrical resistivity is likely small compared to phonon scattering, solute impurity scattering in the Cu matrix and the role of the particle spacing as discussed above. In the microstructural design of recycled Cu, removing the contaminant matrix solutes Fe, Ni, Co, and Mn from the Cu solid solution is thus the main matrix purification step. This necessitates the formation of precipitates driven by sufficiently high chemical potential gradients of the solute elements, enabling their effective segregation and immobilization at relatively low temperatures and short diffusion times – thereby minimizing the thermal energy required for heat treatment [31].

4.2. Yield strength contributions

From a mechanical perspective, pure copper is inherently soft; however, the incorporation of impurity atoms into the Cu lattice enhances its strength via solid solution strengthening. These solute atoms introduce local lattice distortions and compositional inhomogeneities, which impede dislocation motion and thus increase the material's resistance to plastic deformation [61]. GBs act as effective obstacles to dislocation movement; consequently, reducing grain size enhances the strength of the metal following the Hall-Petch relationship [50]. GBs are also a major contributor to resistivity in polycrystalline metals due to their strong scattering of charge carriers [62,63]. GB segregation can also increase or decrease resistivity depending on the impurity element and distribution [64,65]. In the current scenario, we see significant O segregation to GBs for both the Cu450 and Cu550 samples, but this is expected to be rather insignificant at room temperature, where phonon and solute scattering dominate [66]. The GB enrichment is believed to occur via oxygen diffusion to the GB (high chemical affinity between Cu and O makes this favorable) to establish an equilibrium between the grain interior and the GB to lower the system's Gibbs free energy [67]. This leaves the formation of the nanoprecipitates from the solute impurity atoms in the Cu matrix as the most effective balanced hardening and cleaning effect for the current recycled Cu alloys by impeding dislocation motion (i.e., precipitation strengthening) without harming conductivity [31]. The yield strength (σ_y) of the studied alloys originates from cumulative strengthening contributions expressed as:

$$\sigma_y = \sigma_o + \sigma_{gb} + \sigma_d + \sigma_p$$

Where σ_o is the lattice friction stress of Cu, σ_{gb} is the grain boundary strengthening contribution, σ_d is the dislocation strengthening contribution and σ_p is the precipitation-strengthening contribution. The lattice friction stress of Cu is 25 MPa [68].

The strengthening contribution from grain boundaries is expressed as: $\sigma_{gb} = k_y d^{-0.5}$. The Hall-Petch coefficient, k_y is 110 MPa·μm$^{1/2}$ for Cu [68] and d is the average grain size of the matrix. According to the average grain sizes from EBSD, the σ_{gb} for the Cu450 and Cu550 samples are estimated as 27.4 MPa and 18.7 MPa, respectively.

The dislocation strengthening contribution, σ_d is expressed as $\sigma_d = \alpha M G b \sqrt{\rho}$, where α is a geometric constant (0.2), M is the Taylor factor for fcc metals (3.06), G is the shear modulus of Cu (42.1 GPa), b is the magnitude of Burger's vector (0.255 nm) and ρ is the dislocation density. The dislocation densities obtained from the EBSD analysis for the Cu450 and Cu550 samples are 33.97×10^{12}m^{-2} and 23.62×10^{12}m^{-2}, respectively. The dislocation strength is hereafter estimated as σ_d(Cu450) = 38.3 MPa and σ_d(Cu550) = 31.9 MPa.

The precipitation strengthening contribution, σ_p is typically associated with the interactions between dislocations and precipitates, where the dislocations either shear or bypass the precipitates. The precipitate size, volume fraction, shape, orientation, spacing, and coherency with the matrix mainly influence the degree of strengthening. In the current study, we estimate the strengthening contributions of the precipitates as: $\sigma_p = \sigma_y - \sigma_{gb} - \sigma_d - \sigma_o$. σ_p is found to be 47.3 MPa for the Cu450 sample, while a final value of σ_p = 34.3 MPa is obtained for the Cu550 sample.

We acknowledge that Cu is primarily used for its excellent conductivity, but its limited strength complicates microstructural modifications during recycling due to the strength-conductivity tradeoff [31]. Thus, in this scenario, selecting lower annealing temperatures (<450°C) will result in high strength but at the cost of a significant loss in electrical conductivity.

4.3. Recycled Cu in a battery cell

Given the aforementioned oxygen enrichment at GBs and the negligible role of phonon scattering under direct current (DC) conditions, particular emphasis should be placed on evaluating the alternating current (AC) conductivity. In this study, AC conductivity was assessed via electrochemical impedance spectroscopy (EIS) over a frequency range spanning from a few megahertz down to 1 Hz. A pronounced difference in the high-frequency region of the bulk impedance spectra was observed between the Cu450 and Cu550 electrodes. This discrepancy is likely attributed to oxygen enrichment at the grain boundaries, where the formation of oxygen-rich regions induces space charge zones that contribute to increased impedance in the high-frequency regime [69]. This was especially noticeable for Cu450, which has a smaller average grain size. This additional impedance can be minimized when the thickness of the CC is reduced from 150 μm, in this case, to a value comparable to the commercial CC, i.e., 18 μm. Alternatively, via a secondary treatment to remove the trace oxygen trapped in the GBs. A secondary effect that was observed at slow charging speeds was a higher capacity for the case of Cu450. This indicates that these O-rich GBs may also have the possibility to store additional lithium. This is in line with CuO being a conversion-type anode material [70]. Nevertheless, the DC (dis-)charging remains comparable for Cu450 and Cu550, especially at medium charging rates of C/3, which agrees with the previous arguments that phonon scattering and solute scattering are the dominant mechanisms of electron conduction at room temperature. This demonstrates the viability of the recycled material for a second life.

5. Conclusions

From an economic standpoint, a closed-loop recycling framework for battery materials enhances their sustainability by extending the extracted raw material's lifespan. Despite progress in battery recycling, the current operational costs remain high, making it challenging for manufacturers to adopt these practices fully. Another significant challenge lies in meeting the stringent purity requirements for battery materials, which are nearly unattainable when incorporating recycled components into battery production. This limitation arises from the potential risk of compromised material properties. In the case of Cu CCs, 99.99% purity Cu with 97–101% IACS electrical conductivity is the widely accepted operational standard in LIBs [16,47]. However, the main outcome of our study is that 100% recycled Cu, with a significant drop-off in electrical conductivity (~45 to 65% IACS) could still be good enough for reuse as a new battery component, a solution in which closed-loop recycling is achieved. This is made possible by a matrix cleaning effect together with an optimal nanoparticle spacing that balances scattering with strength, as discussed above. Furthermore, recycled copper can also be commercialized in non-electrical applications, including the production of plumbing tubes, roofing sheets, and heat exchangers. These findings highlight that recycling copper from spent

batteries provides a significant secondary resource to bolster the copper supply chain. This approach not only supports the production of new batteries but also contributes to establishing a sustainable and viable circular economy.

CRediT authorship contribution statement

Raymond Kwesi Nutor: Writing – review & editing, Writing – original draft, Formal analysis, Conceptualization. **Martina Ruffino:** Writing – review & editing, Writing – original draft, Formal analysis. **Adam Cohen Miles:** Writing – review & editing, Investigation, Data curation. **Yug Joshi:** Writing – review & editing, Validation, Methodology, Formal analysis, Data curation. **Eric V. Woods:** Writing – review & editing, Software, Formal analysis. **Mohammed Kamran Bhat:** Methodology, Investigation, Data curation. **Syeda Ramin Jannat:** Investigation, Formal analysis, Data curation. **Ubaid Manzoor:** Methodology, Data curation. **Isnaldi R. Souza Filho:** Writing – review & editing, Resources, Funding acquisition, Conceptualization. **Dierk Raabe:** Writing – review & editing, Writing – original draft, Project administration, Funding acquisition, Formal analysis. **Baptiste Gault:** Writing – review & editing, Writing – original draft, Supervision, Resources, Funding acquisition, Conceptualization.

Declaration of competing interest

The authors declare that they have no known competing financial interests or personal relationships that could have appeared to influence the work reported in this paper.

Acknowledgements

We thank Philipp Watermeyer and Dennis Klapproth for the technical support. RKN and BG are grateful for support from the Alexander von Humboldt Stiftung through the award of a fellowship from the Henriette Herz Scouting Program. MR is grateful for the support from the Max-Planck scholarship. EVW and BG are grateful for funding from the DFG through the award of the 2020 Leibniz Prize to BG. A.C.M is grateful for funding from Horizon Europe Project HAlMan under grant agreement number 101091936. UM and DR acknowledge funding by the European Union through the ERC Advanced Grant 'ROC' (grant agreement No 101054368). MKB gratefully acknowledges the funding and support provided by the European Research Council (ERC) under the EU's Horizon 2020 Research and Innovation Program (ERC Advanced Grant, GB-Correlate, Grant No. 787446). Y.J. is grateful for funding from EU Horizon Research and Innovation Actions under grant agreement number 101192848. Views and opinions expressed are, however, those of the author(s) only and do not necessarily reflect those of the European Union or the ERC. Neither the European Union nor the granting authority can be held responsible for them.

Supplementary materials

Supplementary material associated with this article can be found, in the online version, at doi:10.1016/j.actamat.2025.121373.

References

[1] A. Elshkaki, T.E. Graedel, L. Ciacci, B.K. Reck, Copper demand, supply, and associated energy use to 2050, Glob. Environ. Chang. 39 (2016) 305–315, https://doi.org/10.1016/j.gloenvcha.2016.06.006.
[2] J.E. Tilton, G. Lagos, Assessing the long-run availability of copper, Resour. Policy 32 (2007) 19–23, https://doi.org/10.1016/j.resourpol.2007.04.001.
[3] S.K. Haldar, Mineral processing. Mineral Exploration, Elsevier, 2018, pp. 259–290, https://doi.org/10.1016/B978-0-12-814022-2.00013-7.
[4] Lithium Announces Shareholder Approval of Name Change to Reflect its Focus on its 100%-Owned Northern Lights Copper Project Located in Nevada, WTCRF Stock News, 2022. https://www.stocktitan.net/news/WTCRF/li3-lithium-announces-shareholder-approval-of-name-change-to-reflect-jj1sqve78mae.html. accessed November 24, 2024.
[5] A.I. Helped to Spot a Copper Mining Bonanza in Zambia, The New York Times, 2024. https://www.nytimes.com/2024/07/11/climate/kobold-zambia-copper-ai-mining.html?unlocked_article_code=1.6k0._9aI.hlCOXPHJ-9v5&smid=nytcore-ios-share&referringSource=articleShare&sgrp=c-cb. accessed October 14, 2024.
[6] R.B. Gordon, M. Bertram, T.E. Graedel, Metal stocks and sustainability, Proc. Natl. Acad. Sci. USA 103 (2006) 1209–1214, https://doi.org/10.1073/pnas.0509498103.
[7] E.A. Olivetti, J.M. Cullen, Toward a sustainable materials system, Science 360 (2018) 1396–1398, https://doi.org/10.1126/science.aat6821.
[8] D. Raabe, C.C. Tasan, E.A. Olivetti, Strategies for improving the sustainability of structural metals, Nature 575 (2019) 64–74, https://doi.org/10.1038/s41586-019-1702-5.
[9] D. Raabe, The materials science behind sustainable metals and alloys, Chem. Rev. 123 (2023) 2436–2608, https://doi.org/10.1021/acs.chemrev.2c00799.
[10] J. Leiva González, I. Onederra, Environmental management strategies in the copper mining industry in Chile to address water and energy challenges–review, Mining 2 (2022) 197–232, https://doi.org/10.3390/mining2020012.
[11] G.A. Flores, C. Risopatron, J. Pease, Processing of complex materials in the copper industry: challenges and opportunities ahead, JOM 72 (2020) 3447–3461, https://doi.org/10.1007/s11837-020-04255-9.
[12] M.L.C.M. Henckens, E. Worrell, Reviewing the availability of copper and nickel for future generations. The balance between production growth, sustainability and recycling rates, J. Clean. Prod. 264 (2020) 121460, https://doi.org/10.1016/j.jclepro.2020.121460.
[13] G.S. Seck, E. Hache, C. Bonnet, M. Simoën, S. Carcanague, Copper at the crossroads: assessment of the interactions between low-carbon energy transition and supply limitations, Resour. Conserv. Recycl. 163 (2020) 105072, https://doi.org/10.1016/j.resconrec.2020.105072.
[14] G. Harper, R. Sommerville, E. Kendrick, L. Driscoll, P. Slater, R. Stolkin, A. Walton, P. Christensen, O. Heidrich, S. Lambert, A. Abbott, K. Ryder, L. Gaines, P. Anderson, Recycling lithium-ion batteries from electric vehicles, Nature 575 (2019) 75–86, https://doi.org/10.1038/s41586-019-1682-5.
[15] G. Azimi, K.H. Chan, A review of contemporary and emerging recycling methods for lithium-ion batteries with a focus on NMC cathodes, Resour. Conserv. Recycl. 209 (2024) 107825, https://doi.org/10.1016/j.resconrec.2024.107825.
[16] P. Zhu, D. Gastol, J. Marshall, R. Sommerville, V. Goodship, E. Kendrick, A review of current collectors for lithium-ion batteries, J. Power Sources 485 (2021) 229321, https://doi.org/10.1016/j.jpowsour.2020.229321.
[17] Official Site of Copper Development Association, Inc. (USA), (2024). https://www.copper.org/ (accessed October 30, 2024).
[18] H. Takimoto, S. Kosai, T. Watari, E. Yamasue, Circular economy can mitigate rising mining demand from global vehicle electrification, Resour. Conserv. Recycl. 209 (2024) 107748, https://doi.org/10.1016/j.resconrec.2024.107748.
[19] E. Drabik, V. Rizos, Prospects for electric vehicle batteries in a circular economy. CEPS Research Report No 2018/05, July 2018, 2018. http://aei.pitt.edu/id/eprint/94326.
[20] J. Gardiner, The rise of electric cars could leave us with a big battery waste problem. Guardian Sustainable Business, The Guardian, 2017. Guard, https://www.theguardian.com/sustainable-business/2017/aug/10/electric-cars-big-battery-waste-problem-lithium-recycling. accessed October 14, 2024.
[21] Calls rise for lithium-ion battery regulations as fires multiply, (2023). https://www.axios.com/2023/03/31/battery-fires-regulation-new-york-city-lithium-ion (accessed October 14, 2024).
[22] COM.798.final, Regulation of the European Parliament and of the Council concerning batteries and waste batteries, repealing. Directive 2006/66/EC and amending Regulation (EU) No 2019/1020, 2020. https://eur-lex.europa.eu/legal-content/EN/TXT/?uri=CELEX%3A52020PC0798.
[23] C.B. Tabelin, I. Park, T. Phengsaart, S. Jeon, M. Villacorte-Tabelin, D. Alonzo, K. Yoo, M. Ito, N. Hiroyoshi, Copper and critical metals production from porphyry ores and E-wastes: a review of resource availability, processing/recycling challenges, socio-environmental aspects, and sustainability issues, Resour. Conserv. Recycl. 170 (2021) 105610, https://doi.org/10.1016/j.resconrec.2021.105610.
[24] H. Tian, Z. Guo, J. Pan, D. Zhu, C. Yang, Y. Xue, S. Li, D. Wang, Comprehensive review on metallurgical recycling and cleaning of copper slag, Resour. Conserv. Recycl. 168 (2021) 105366, https://doi.org/10.1016/j.resconrec.2020.105366.
[25] Y. Liu, J. Zhang, R. Niu, M. Bayat, Y. Zhou, Y. Yin, Q. Tan, S. Liu, J.H. Hattel, M. Li, X. Huang, J. Cairney, Y.S. Chen, M. Easton, C. Hutchinson, M.X. Zhang, Manufacturing of high strength and high conductivity copper with laser powder bed fusion, Nat. Commun. 15 (2024) 1283, https://doi.org/10.1038/s41467-024-45732-y.
[26] A.H. Kaksonen, L. Lavonen, M. Kuusenaho, A. Kolli, H. Närhi, E. Vestola, J. A. Puhakka, O.H. Tuovinen, Bioleaching and recovery of metals from final slag waste of the copper smelting industry, Miner. Eng. 24 (2011) 1113–1121, https://doi.org/10.1016/j.mineng.2011.02.011.
[27] W.R. Wampler, T. Schober, B. Lengeler, Precipitation and trapping of hydrogen in copper, Philos. Mag. 34 (1976) 129–141, https://doi.org/10.1080/14786437608228179.
[28] Y. Zhu, K. Mimura, M. Isshiki, Oxidation mechanism of copper at 623-1073 K, Mater. Trans. 43 (2002) 2173–2176, https://doi.org/10.2320/matertrans.43.2173.
[29] M.J. Balart, J.B. Patel, F. Gao, Z. Fan, Grain refinement of deoxidized copper, Metall. Mater. Trans. A 47 (2016) 4988–5011, https://doi.org/10.1007/s11661-016-3671-8.

[30] J.S. Liu, W.X. Yu, D.Y. Chen, S.W. Wang, H.W. Song, S.H. Zhang, A review of studies on the influence of rare-earth elements on the microstructures and properties of copper and copper alloys and relevant applications, Metals 15 (2025) 536, https://doi.org/10.3390/met15050536.
[31] K. Yang, Y. Wang, M. Guo, H. Wang, Y. Mo, X. Dong, H. Lou, Recent development of advanced precipitation-strengthened Cu alloys with high strength and conductivity: a review, Prog. Mater. Sci. 138 (2023) 101141, https://doi.org/10.1016/j.pmatsci.2023.101141.
[32] W.D. Riley, H.V. Makar, Impurity effects in secondary copper alloys, Conserv. Recycl. 9 (1986) 315–323, https://doi.org/10.1016/0361-3658(86)90066-4.
[33] D.G.R. William, D. Callister Jr., Materials Science and Engineering, An Introduction, 9th ed., Wiley, New York, 2009.
[34] M.F. Börner, M.H. Frieges, B. Späth, K. Spütz, H.H. Heimes, D.U. Sauer, W. Li, Challenges of second-life concepts for retired electric vehicle batteries, Cell Rep. Phys. Sci. 3 (2022) 101095, https://doi.org/10.1016/j.xcrp.2022.101095.
[35] Y. Kotak, C. Marchante Fernández, L. Canals Casals, B.S. Kotak, D. Koch, C. Geisbauer, L. Trilla, A. Gómez-Núñez, H.G. Schweiger, End of electric vehicle batteries: reuse vs. recycle, Energies 14 (2021) 2217, https://doi.org/10.3390/en14082217.
[36] B. Niu, E. Shanshan, Q. Song, Z. Xu, B. Han, Y. Qin, Physicochemical reactions in e-waste recycling, Nat. Rev. Chem. 8 (2024) 569–586, https://doi.org/10.1038/s41570-024-00616-z.
[37] J.J.M.M. van de Ven, Y. Yang, S.T. Abrahami, A closer look at lithium-ion batteries in E-waste and the potential for a universal hydrometallurgical recycling process, Sci. Rep. 14 (2024) 16661, https://doi.org/10.1038/s41598-024-67507-7.
[38] R. Sommerville, J. Shaw-Stewart, V. Goodship, N. Rowson, E. Kendrick, A review of physical processes used in the safe recycling of lithium ion batteries, Sustain. Mater. Technol. 25 (2020) e00197, https://doi.org/10.1016/j.susmat.2020.e00197.
[39] D. Vaumousse, A. Cerezo, P.J. Warren, A procedure for quantification of precipitate microstructures from three-dimensional atom probe data, Ultramicroscopy 95 (2003) 215–221, https://doi.org/10.1016/S0304-3991(02)00319-4.
[40] I.J. van Der Pauw, A method of measuring the resistivity and Hall coefficient on lamellae of arbitrary shape, Philips Tech. Rev. 20 (1958) 220–224.
[41] H. Bishara, M. Ghidelli, G. Dehm, Approaches to measure the resistivity of grain boundaries in metals with high sensitivity and spatial resolution: a case study employing Cu, ACS Appl. Electron. Mater. 2 (2020) 2049–2056, https://doi.org/10.1021/acsaelm.0c00311.
[42] X. Zhao, S. Niketic, C.H. Yim, J. Zhou, J. Wang, Y. Abu-Lebdeh, Revealing the role of poly(vinylidene fluoride) binder in Si/graphite composite anode for Li-ion batteries, ACS Omega 3 (2018) 11684–11690, https://doi.org/10.1021/acsomega.8b01388.
[43] B. Gault, A. Chiaramonti, O. Cojocaru-Mirédin, P. Stender, R. Dubosq, C. Freysoldt, S.K. Makineni, T. Li, M. Moody, J.M. Cairney, Atom probe tomography, Nat. Rev. Methods Prim. 1 (2021) 51, https://doi.org/10.1038/s43586-021-00047-w.
[44] O.C. Hellman, J.A. Vandenbroucke, J. Rüsing, D. Isheim, D.N. Seidman, Analysis of three-dimensional atom-probe data by the proximity histogram, Microsc. Microanal. 6 (2000) 437–444, https://doi.org/10.1007/S100050010051.
[45] J.H. Lee, H.M. Lee, S. Ahn, Battery dimensional changes occurring during charge/discharge cycles–Thin rectangular lithium ion and polymer cells, J. Power Sources 119–121 (2003) 833–837, https://doi.org/10.1016/S0378-7753(03)00281-7.
[46] Q. Shi, C. Lu, Y. Cao, Y. Hao, A. Bachmatiuk, M.H. Rümmeli, Recent developments in current collectors for lithium metal anodes, Mater. Chem. Front. 7 (2023) 1298–1311, https://doi.org/10.1039/D3QM00029J.
[47] C. Lamiel, I. Hussain, X. Ma, K. Zhang, Properties, functions, and challenges: current collectors, Mater. Today Chem. 26 (2022) 101152, https://doi.org/10.1016/j.mtchem.2022.101152.
[48] J. Zhu, J. Feng, Z. Guo, Mechanical properties of commercial copper current-collector foils, RSC Adv. 4 (2014) 57671–57678, https://doi.org/10.1039/C4RA07675C.
[49] Y. Zhang, S. Jing, H. Shen, S. Li, Y. Huang, Y. Shen, S. Liu, Z. Zhang, F. Liu, Developments, novel concepts, and challenges of current collectors: from conventional lithium batteries to all-solid-State batteries, ChemElectroChem 11 (2024), https://doi.org/10.1002/celc.202300739.
[50] N.J. Petch, The cleavage strength of polycrystals, J. Iron Steel Inst. 174 (1953) 25–28.
[51] A. Ahmadian, D. Scheiber, X. Zhou, B. Gault, C.H. Liebscher, L. Romaner, G. Dehm, Aluminum depletion induced by co-segregation of carbon and boron in a bcc-iron grain boundary, Nat. Commun. 12 (2021) 6008, https://doi.org/10.1038/s41467-021-26197-9.
[52] R. Monzen, M.L. Jenkins, A.P. Sutton, The bcc-to-9R martensitic transformation of Cu precipitates and the relaxation process of elastic strains in an Fe-Cu alloy, Philos. Mag. A 80 (2000) 711–723, https://doi.org/10.1080/01418610008212077.
[53] P.T. Coleridge, Impurity scattering in copper, J. Phys. F Met. Phys. 2 (1972) 1016–1032, https://doi.org/10.1088/0305-4608/2/6/007.
[54] J. Freudenberger, H. Warlimont, Copper and copper alloys, in: W. Warlimont, H. Martienssen (Eds.), Springer Handbook of Materials Data. Springer Handbooks., 2nd ed., Springer Nature Switzerland AG, 2018, pp. 297–305, https://doi.org/10.1007/978-3-319-69743-7_12.
[55] T.P. Beaulac, P.B. Allen, F.J. Pinski, Electron-phonon effects in copper. II. Electrical and thermal resistivities and hall coefficient, Phys. Rev. B 26 (1982) 1549–1558, https://doi.org/10.1103/PhysRevB.26.1549.
[56] D. Gall, Electron mean free path in elemental metals, J. Appl. Phys. 119 (2016), https://doi.org/10.1063/1.4942216.
[57] D. Raabe, Simulation of the resistivity of heavily cold worked Cu-20 wt.%Nb wires, Comput. Mater. Sci. 3 (1995) 402–412, https://doi.org/10.1016/0927-0256(94)00079-R.
[58] H. Bishara, S. Lee, T. Brink, M. Ghidelli, G. Dehm, Understanding grain boundary electrical resistivity in Cu: the effect of boundary structure, ACS Nano 15 (2021) 16607–16615, https://doi.org/10.1021/acsnano.1c06367.
[59] B.A. Cook, M.J. Kramer, X. Wei, J.L. Harringa, E.M. Levin, Nature of the cubic to rhombohedral structural transformation in (AgSbTe2)15(GeTe)85 thermoelectric material, J. Appl. Phys. 101 (2007), https://doi.org/10.1063/1.2645675.
[60] L. Lu, Y. Shen, X. Chen, L. Qian, K. Lu, Ultrahigh strength and high electrical conductivity in copper, Science 304 (2004) 422–426, https://doi.org/10.1126/science.1092905.
[61] A.H. Huang, Y.F. Wang, M.S. Wang, L.Y. Song, Y.S. Li, L. Gao, C.X. Huang, Y. T. Zhu, Optimizing the strength, ductility and electrical conductivity of a Cu-Cr-Zr alloy by rotary swaging and aging treatment, Mater. Sci. Eng. A 746 (2019) 211–216, https://doi.org/10.1016/j.msea.2019.01.002.
[62] P.V. Andrews, Resistivity due to grain boundaries in pure copper, Phys. Lett. 19 (1965) 558–560, https://doi.org/10.1016/0031-9163(65)90776-6.
[63] I. Nakamichi, Electrical resistivity and grain boundaries in metals, Mater. Sci. Forum 207–209 (1996) 47–58, https://doi.org/10.4028/www.scientific.net/MSF.207-209.47.
[64] G. Kim, X. Chai, L. Yu, X. Cheng, D.S. Gianola, Interplay between grain boundary segregation and electrical resistivity in dilute nanocrystalline Cu alloys, Scr. Mater. 123 (2016) 113–117, https://doi.org/10.1016/j.scriptamat.2016.06.008.
[65] R. Bueno Villoro, M. Wood, T. Luo, H. Bishara, L. Abdellaoui, D. Zavanelli, B. Gault, G.J. Snyder, C. Scheu, S. Zhang, Fe segregation as a tool to enhance electrical conductivity of grain boundaries in Ti(Co,Fe)Sb half heusler thermoelectrics, Acta Mater. 249 (2023) 118816, https://doi.org/10.1016/j.actamat.2023.118816.
[66] H. Bishara, L. Langenohl, X. Zhou, B. Gault, J.P. Best, G. Dehm, Decoupling the electrical resistivity contribution of grain boundaries in dilute Fe-alloyed Cu thin films, Scr. Mater. 230 (2023) 115393, https://doi.org/10.1016/j.scriptamat.2023.115393.
[67] T.G. Nieh, W.D. Nix, Embrittlement of copper due to segregation of oxygen to grain boundaries, Metall. Trans. A 12 (1981) 893–901, https://doi.org/10.1007/BF02648354.
[68] A.P. Zhilyaev, I. Shakhova, A. Morozova, A. Belyakov, R. Kaibyshev, Grain refinement kinetics and strengthening mechanisms in Cu–0.3Cr–0.5Zr alloy subjected to intense plastic deformation, Mater. Sci. Eng. A 654 (2016) 131–142, https://doi.org/10.1016/j.msea.2015.12.038.
[69] R.A. De Souza, E.C. Dickey, The effect of space-charge formation on the grain-boundary energy of an ionic solid, Philos. Trans. R. Soc. A Math. Phys. Eng. Sci. 377 (2019) 20180430, https://doi.org/10.1098/rsta.2018.0430.
[70] K. Chen, D. Xue, S. Komarneni, Beyond theoretical capacity in Cu-based integrated anode: insight into the structural evolution of CuO, J. Power Sources 275 (2015) 136–143, https://doi.org/10.1016/j.jpowsour.2014.11.002.